Degenerate Rabi spectroscopy of the Floquet engineered optical lattice clock

Wei-Xin Liu,[1] Xiao-Tong Lu,[2,3] Ting Li,[2,3] Xue-Feng Zhang ●,[4,5] Hong Chang,[2,3] Tao Wang ●,[4,6,5,*] and Wei-Dong Li[7]

[1]*Institute of Theoretical Physics and Department of Physics, State Key Laboratory of Quantum Optics and Quantum Optics Devices,*
Collaborative Innovation Center of Extreme Optics, Shanxi University, Taiyuan 030006, China

[2]*Key Laboratory of Time and Frequency Primary Standards, National Time Service Center,*
Chinese Academy of Sciences, Xi'an 710600, China

[3]*School of Astronomy and Space Science, University of Chinese Academy of Sciences, Beijing 100049, China*

[4]*Department of Physics and Center of Quantum Materials and Devices, Chongqing University, Chongqing 401331, China*

[5]*Chongqing Key Laboratory for Strongly Coupled Physics, Chongqing University, Chongqing 401331, China*

[6]*Center of Modern Physics, Institute for Smart City of Chongqing University in Liyang, Liyang 213300, China*

[7]*Shenzhen Key Laboratory of Ultraintense Laser and Advanced Material Technology,*
Center for Advanced Material Diagnostic Technology, and College of Engineering Physics,
Shenzhen Technology University, Shenzhen 518118, China

Simulating physics with large SU(N) symmetry is one of the unique advantages of alkaline-earth-metal atoms. Introducing periodical driving modes to the system may provide richer SU(N) physics that the static one cannot reach. However, a discussion of whether or not the driving modes will break the SU(N) symmetry is still lacking. Here we experimentally study a Floquet engineered degenerate ^{87}Sr optical lattice clock (OLC) by periodically modulating the frequency of the lattice laser. With the help of Rabi spectroscopy, we find that the atoms at different Zeeman sublevels are tuned by the same driven function. Meanwhile, our experimental results suggest that the uniform distribution among the sublevels does not change despite the driving. Our experimental demonstrations may pave the way for implementation of Floquet engineering on tailoring the SU(N) physics in the OLC system.

I. INTRODUCTION

Alkaline-earth-metal atoms (AEAs; along with the alkaline-earth-metal-like atom Yb), with their unique atomic structures, have become a hot frontier in ultracold-atom physics. The ultranarrow doubly forbidden transition between the ground state $^1S_0$ and the excited state $^3P_0$ (which can be called the two clock states) makes the AEAs ideal for the realization of ultraprecise atomic clocks. State-of-the-art optical lattice clocks (OLCs) using ultracold AEAs have surpassed the best ^{133}Cs primary standards [1–5]. Meanwhile, owing to the strong decoupling between the nuclear spin I and the electronic angular momentum $J = 0$ of the two lowest electronic states $^1S_0$ and $^3P_0$, AEAs show that the nuclear spin is independent of both interatomic collision and trapping potential. This property directly leads to the SU($N \leqslant 2I + 1$) symmetry emerging in AEAs [6–21]. AEAs possessing high-dimensional symmetries with large N (e.g., 10 for ^{87}Sr) have been predicted to simulate high-energy lattice gauge theories [14] but also are a unique platform for investigating a variety of many-body phases [22–25]. Recently, more and more experiments have supported the existence of the SU(N) symmetry [8,9,11,26–28].

On the other hand, increasing efforts have been devoted to manipulating ultracold atoms using time-periodic modulations. Focusing on the optical lattice, the modulation can provide an extremely clean system with high controllability in a time-dependent fashion. This coherent manipulation of the quantum system is known as Floquet engineering (FE) [29]. FE of ultracold atoms in an optical lattice shows high potential for simulating and studying a wide variety of condensed-matter systems and even some models in high-energy physics. It has led to many successes, such as dynamic control of the insulator-superfluid quantum phase transition [30], the realization of the topological band structure [31–33], and the creation of artificial gauge fields [34–37]. Thus, introducing FE into the SU(N) physics of AEA Fermi gases has become more attractive, including renormalizing the tunneling of the SU(N) Hubbard model or generating the exotic SU(N) phase [38]. However, the compatibility of FE with the SU(N) symmetry needs to be addressed first before these impressive prospects are pursued. For example, periodically modulating an optical lattice means adding an extra time-dependent electromagnetic field to the system, which might enhance the admixture between $^3P_0$ and higher-lying P states with $J \neq 0$ and thereby break SU(N) symmetry [7]. Thus, it is interesting to ask the following questions: will atoms at different sublevels be tuned by the same driving function, and will the uniform distribution among sublevels be changed by periodic driving?

In this paper, we experimentally realize a Floquet engineered degenerate clock transition in a one-dimensional (1D) ^{87}Sr OLC and also demonstrate that FE does not apparently
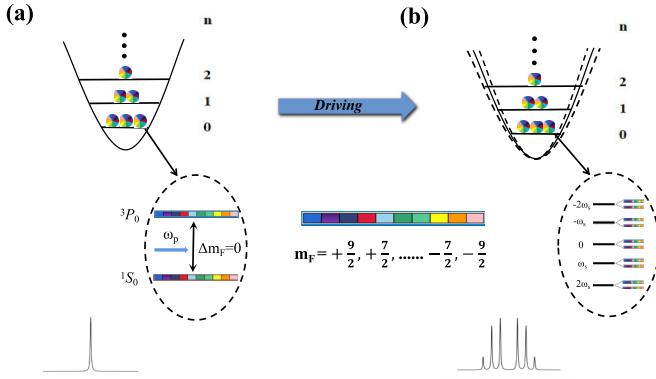
(a)

(b)

FIG. 1. Floquet engineered degenerate optical lattice clock. In the absence of magnetic field, both clock states have 10 degenerate sublevels (denoted by different colors [11]). (a) Without driving, the atoms follow the Boltzmann distribution in the external states. After the π clock transitions, the atoms can hop between two clock states without changing their Zeeman sublevels $\Delta m_F = 0$. (b) Under the lattice driving pattern, the carrier peak in Rabi spectroscopy can split into several Floquet sidebands. Each Floquet sideband corresponds to the π clock transitions in each Floquet energy level which can still retain the SU(N) symmetry.

change the distribution of atoms among degenerate energy levels with the help of Rabi spectroscopy. As shown in Fig. 1, fermionic ^{87}Sr has a nuclear spin of $I = 9/2$; therefore, both clock states have tenfold degeneracy ($2F + 1 = 10$, where $F = I + J$ is the total atomic angular momentum) in the absence of magnetic field, corresponding to the 10 Zeeman sublevels from $m_F = -9/2$ to $m_F = 9/2$ (m_F is the magnetic quantum number of the total angular momentum). Then, all 10 degenerate sublevels can be Floquet engineered by modulating the lattice laser around the "magic" wavelength in a nearly zero magnetic field. Under this driving pattern, the internal dynamics of the π transition in each m_F sublevel is governed by the time-dependent Landau-Zener-Stückelberg-Majorana Hamiltonian due to the Doppler effect [39–41]. The total clock-transition probability can be theoretically calculated based on the resolved Floquet sideband approximation [39,42]. After extracting the experimental parameters in the nondriven case, especially the bare Rabi frequencies of all sublevels, we estimate the residual stray magnetic field. Last, we measure the Floquet degenerate Rabi spectrum and the Rabi oscillation and find the periodic modulation will not break the SU(N) symmetry.

This paper is organized as follows. In Sec. II, we briefly introduce the experimental setup. In Sec. III, we give the model of the degenerate driven system and its analytic solution. In Sec. IV, we discuss how to determine the experimental parameters. In Sec. V, we demonstrate the degenerate Floquet Rabi spectroscopy and give an analysis of the SU(N) symmetry. Section VI includes the conclusions and outlook.

II. EXPERIMENTAL SETUP

Approximately 10^4 ^{87}Sr atoms are cooled to about 3 μK using standard laser-cooling techniques and trapped in a 1D optical lattice in the Lamb-Dicke region, where the mo-

tion and the photon recoil momentum of the atom will not broaden the clock-transition spectra [43–45]. The 1D optical lattice consists of two counterpropagating laser beams at the magic wavelength $\lambda_L = 813.43$ nm [45], where the ac Stark frequency shifts of the two clock states $(5s^2)\,^1S_0$ ($|g\rangle$) and $(5s5p)\,^3P_0$ ($|e\rangle$) are identical. One incident lattice laser beam, with a linear polarization along the direction of gravity, is focused on the center of the magneto-optical trap (MOT). After a high-reflection mirror, its retroreflected laser beam is also focused on the MOT center and forms a standing wave with the incident laser. The lattice laser (TOPTICA Photonics AG, Munich, Germany) has a power of 300 mW and beam waist $w_0 \simeq 50$ μm around the MOT center. Because of the large trapping depth $U_0 \simeq 94E_R$ in our experiments, where E_R is the lattice recoil energy (see the Appendix), the tunneling between lattice sites can be ignored, so that the system can be taken as a series of independent harmonic traps. The eigenstates of each harmonic trap are labeled as the external states $|\vec{n}\rangle$ or $|n_r, n_z\rangle$, where $n_{r(z)}$ corresponds to the transverse (longitudinal) direction of the optical lattice potential [39,46].

The clock transition $^1S_0 \leftrightarrow\,^3P_0$ is interrogated by the clock laser (DL Pro, TOPTICA Photonics AG, Munich, Germany) with a wavelength of 698 nm propagating collinear with the lattice laser. The clock laser is divided into two parts by a beam splitter (BS). Ninety percent of the clock laser passes directly through the BS, is collimated by the lens assembly, and overlaps with the lattice laser. Ten percent is reflected by the BS and then enters a 10-cm-long ultralow-expansion ultrastable cavity with a finesse of 400 000. The clock laser beam has the same polarization direction as the lattice laser, with a 2-mm waist around the MOT center. The linewidth of the clock laser is narrowed to 1 Hz after Pound-Drever-Hall locking, and the short-term stability of the clock laser is 1×10^{-15} at 1 s [47]. The natural lifetime of $^3P_0$ is about 120 s, and the duration of the measurement processes does not exceed 1 s, so we can ignore the spontaneous emission during the clock-transition detection by using the method of "electronic shelving" [45,48].

By changing the currents of three-dimensional compensation coils (TDCCs), we fine-tune the magnetic field around the atoms approaching zero as much as possible. Then we apply a periodic sinusoidal modulation to the piezoelectric transducer (PZT) attached to the grating of the external cavity which generates the lattice light to periodically change the cavity length. Under this modulation, the lattice frequency is modulated accordingly and can be expressed as $\omega_L(t) = \bar{\omega}_L + \omega_a \sin(\omega_s t)$, where $\bar{\omega}_L = 2\pi c/\lambda_L$ is the central lattice frequency at the magic wavelength λ_L and $\omega_{a(s)}$ is the driving amplitude (frequency), which is typically several hundred megahertz (hertz) in our experiment. The degenerate driving spectra can be obtained by scanning the frequency of the clock laser with the help of an acousto-optic modulator in each clock detection cycle. The intensity of the clock laser is set to be $I_p \simeq 3$ μW/cm^2, which gives a power broadened transition linewidth $\gamma\sqrt{1 + I_p/I_{\text{sat}}} \simeq 2.7$ Hz, with $I_{\text{sat}} = 0.41$ pW/cm^2 being the saturation intensity of the clock transition and $\gamma = 1$ mHz being the natural linewidth [45]. Considering the Fourier-limited linewidth of the Rabi spectrum is $0.89/t \simeq 5.9$ Hz with $t = 150$ ms, which is the main limit of the spectrum linewidth, we can neglect the effect of saturation broadening.

III. THE MODEL

Under the lattice laser frequency modulation, the atoms at different sublevels may pick up a sublevel-dependent velocity in the comoving frame of the lattice [39]. Due to the Doppler effect, the dynamics of the atoms at certain m_F in external energy level $|\vec{n}\rangle$ is governed by the time-dependent Landau-Zener-Stückelberg-Majorana Hamiltonian in the lattice comoving frame [39–41]

$$\hat{H}_{\vec{n}}^{m_F}(t) = \frac{\hbar}{2}\left[\delta_{m_F} + A_{m_F}\omega_s \cos(\omega_s t)\right]\hat{\sigma}_z + \frac{\hbar}{2}g_{\vec{n}}^{m_F}\hat{\sigma}_x. \quad (1)$$

Here $\hbar$ is the reduced Planck's constant, and the detuning $\delta_{m_F} = \delta + \Delta\omega_0^{m_F}$ includes the bare clock-laser detuning $\delta = \omega_p - \omega_0$ and also the π-transition frequency shift for the m_F sublevel $\Delta\omega_0^{m_F}$ because there is still an unavoidable small residual magnetic field in the experiment. ω_0 and ω_p are the bare clock-transition frequency and clock-laser frequency, respectively. A_{m_F} is the sublevel-dependent renormalized driving amplitude, and $g_{\vec{n}}^{m_F}$ is the coupling strength of the m_F sublevel in the external state $|\vec{n}\rangle$ [39,46].

The π-transition frequency shift is derived from the as Stark shift caused by the lattice laser acting on the Zeeman sublevels and the possible residual stray magnetic field. In the present of lattice potential with trapping depth U_0 at a weak magnetic field B, the π-transition frequency shift between m_F sublevels can be expressed as [49–51]

$$\Delta\omega_0^{m_F} = (\Delta\kappa^S + \Delta\kappa^V m_F \xi \vec{e}_k \cdot \vec{e}_B + \Delta\kappa^T \beta)U_0 + \delta g m_F \mu_0 B, \quad (2)$$

where $\Delta\kappa^S$, $\Delta\kappa^V$, and $\Delta\kappa^T$ are the coefficients due to differential scalar, vector, and tensor polarizabilities between $^1S_0$ and $^3P_0$, respectively. ξ is the degree of ellipticity of the lattice light field, where $\xi = 0$ (± 1) represents perfect linear (circular) polarization. $\vec{e}_B$ and $\vec{e}_k$ are unitary vectors along the quantization axis and the lattice wave vector, respectively. The coefficient β is equal to $(3\cos^2\phi - 1)[3m_F^2 - F(F+1)]$, with ϕ being the angle between the linear polarization direction of the lattice laser and the quantization axis. The last term in Eq. (2) is the first-order Zeeman shift in which δg is the differential Landé factor between the two clock states due to the hyperfine interaction on the excited state $^3P_0$ [49,52]. μ_0 is equal to μ_B/h, with μ_B being the Bohr magneton and h being Planck's constant. The hyperpolarizability effect ($\propto U_0^2$) and the second-order Zeeman shift are ignored in Eq. (2) as they are negligible at the level of 1 mHz [51,53–55].

First, the effect of scalar shift can be neglected because it is independent of m_F while the lattice laser frequency varies around the magic wavelength. Second, the effect of periodic driving on the external potential can also be neglected due to the small driving amplitude [39]. Third, considering the lattice field is linearly polarized along the quantization axis, we can directly obtain $\xi \simeq 0$, $\vec{e}_k \cdot \vec{e}_B \simeq 0$, and $\phi \simeq 0$, so the vector shift term is also omitted. Last, according to Ref. [51], the tensor shift coefficient is about -0.06 mHz/E_R. Because $U_0 \simeq 94E_R$ in our experiment (see the Appendix), the tensor shift is less than 1 Hz and can also be neglected. Thus, the main frequency shift is only the last term, which depends on m_F and the magnetic field B, with $\delta g\mu_0 = -108.4(4)$ Hz/G [49].

TABLE I. The determined experimental parameters.

Parameter	Value	Parameter	Value	Parameter	Value
T_z	3.5 μK	ν_z	66.8 kHz	N_z	5
T_r	4.0 μK	ν_r	250 Hz	N_r	1336

Then, the π-transition frequency shift can be simplified as $\Delta\omega_0^{m_F} = -108.4 m_F B$.

The population of atoms is evenly distributed among 10 Zeeman sublevels after the second stage of cooling [56]. In the absence of driving, SU($N = 10$) symmetry implies the number of atoms in each of the 10 sublevels is conserved [11,26]. The dynamics of atom distribution due to the FE is still an open question, so here we introduce a sublevel-dependent distribution N_{m_F}/N_0 during the FE, where N_0 is the total atom number and it will be determined from the experiments later. The Floquet spectrum can be treated as the summation of contributions from all the independent degenerated sublevels, so the total excitation probability in terms of the Zeeman sublevels can be obtained by solving the Hamiltonian (1) with the resolved Floquet sideband approximation [39,42]

$$P_e^{\text{Tol}} = \sum_{m_F} P_e^{m_F}, \quad (3)$$

where

$$P_e^{m_F} = \sum_{\vec{n},k} q(\vec{n})\left[\frac{N_{m_F}g_{\vec{n}}^{m_F}J_k(A_{m_F})}{N_0 g_{\text{eff}}^{k,m_F}}\right]^2 \sin^2\left(\frac{g_{\text{eff}}^{k,m_F}}{2}t\right) \quad (4)$$

is the excitation probability of the m_F sublevel and

$$g_{\text{eff}}^{k,m_F} = \sqrt{\left(\delta_{m_F} - k\omega_s\right)^2 + \left[g_{\vec{n}}^{m_F}J_k(A_{m_F})\right]^2} \quad (5)$$

is the effective Rabi frequency for the kth-order sideband of the m_F sublevel, $J_k(\cdot)$ is the kth-order Bessel function of the first kind, and $q(\vec{n})$ is the Boltzmann factor. The coupling strength can be explicitly written as $g_{\vec{n}}^{m_F} = g_{m_F}e^{-\eta_z^2/2}e^{-\eta_r^2/2}L_{n_z}(\eta_z^2)L_{n_r}(\eta_r^2)$, where $\eta_z = \sqrt{h/(2m\nu_z)}/\lambda_p$ and $\eta_r = \sqrt{h/(2m\nu_r)}\Delta\theta/\lambda_p$ are the Lamb-Dicke parameters, $\nu_{z(r)}$ is the longitudinal (transverse) trap frequency, λ_p is the clock-laser wavelength, $\Delta\theta$ is the residual misalignment angle between the lattice and probe axis, and m is the mass of the atom [39,46]. In order to theoretically obtain the excitation probability [39,40,57], the experimental parameters should be determined first.

IV. DETERMINATION OF THE EXPERIMENTAL PARAMETERS

In the nondriven case, the SU(N) symmetry is not broken, so $N_{m_F}/N_0 = 1/N$. Then we can determine the experimental parameters from the degenerate Rabi spectrum in the nondriven system. In Table I, we list some of the determined experimental parameters which require the same methods as the polarized case (see Ref. [39] and the Appendix). Besides that, we need to determine the bare Rabi frequencies g_{m_F} of
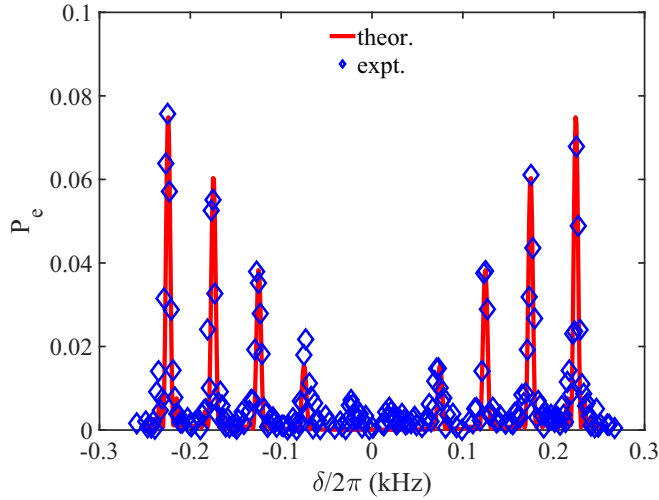
FIG. 2. The Zeeman spectrum in the presence of a 460-mG magnetic field at 150-ms clock-laser interrogation time. These peaks, from left to right, correspond to the π transition for the $m_F = -9/2$ to $m_F = +9/2$ sublevels, respectively.
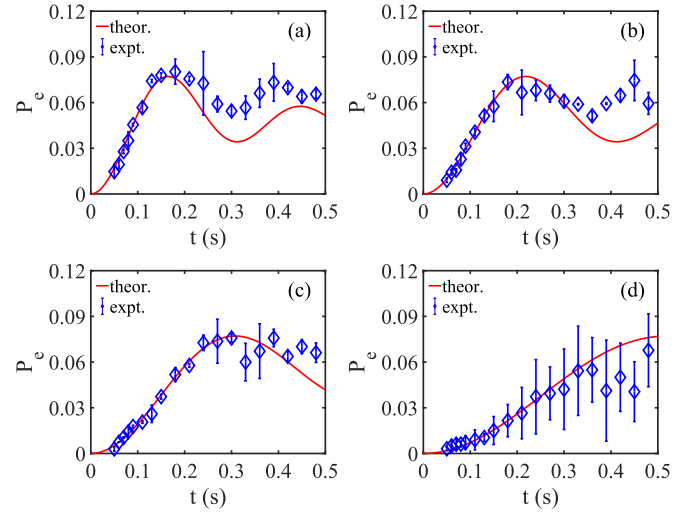

FIG. 3. Rabi oscillations of different Zeeman sublevels at (a) $|m_F| = 9/2$, (b) $|m_F| = 7/2$, (c) $|m_F| = 5/2$, and (d) $|m_F| = 3/2$. The experimental parameters are the same as in Fig. 2.

all the sublevels as well as the small residual magnetic field B without driving.

First, we use the nondriven Zeeman spectrum to extract the Rabi frequency of each sublevel. In order to split the Zeeman sublevels, the currents of TDCCs are adjusted to as large as 460 mG along the direction of gravity. As shown in Fig. 2, the Zeeman spectrum presents eight obvious peaks with intervals close to the theoretical prediction $\delta\Delta\omega_0^{m_F} = 108.4B \approx 50$ Hz, which is much larger than linewidths of the spectrum that are a few hertz. Due to the first-order Zeeman shift, these peaks correspond to the Zeeman sublevels except for $m_F = \pm 1/2$, which has a quite weak excitation probability. By scanning the clock-laser frequency at a fixed clock-laser interrogation time, we get a set of Zeeman spectra in Fig. 2. Then we can extract the excitation fraction for each sublevel from the Zeeman spectra under different interrogation times and get the Rabi oscillations of the sublevels as shown in Figs. 3(a)–3(d), corresponding to $|m_F| = 9/2, 7/2, 5/2, 3/2$, respectively. In order to improve the experimental data, here we take the average of sublevels with the same $|m_F|$ due to positive-negative or $\mathbb{Z}_2$ symmetry. In addition, the Rabi oscillation of sublevel $|m_F| = 1/2$ is not shown here because it is too small, and we also ignore its effect on the Floquet spectra in the following. Then by fitting the experimental data (before the 200-ms interrogation time) for each Zeeman sublevel with Eq. (4) while taking $A_{m_F} = 0$, $\omega_s = 0$, and $N_{m_F}/N_0 = 1/N$, we can get the Rabi frequency $g_{|m_F|}$ in each sublevel and the misalignment angle $\Delta\theta$, which should be the same for all sublevels [39,46]. Then, the fitting results are $g_{\pm 9/2}/2\pi = 4.1$ Hz, $g_{\pm 7/2}/2\pi = 3.1$ Hz, $g_{\pm 5/2}/2\pi = 2.2$ Hz, and $g_{\pm 3/2}/2\pi = 1.3$ Hz at a fixed average misalignment angle $\overline{\Delta\theta} = 8$ mrad. With the help of these Rabi frequencies, we show the theoretical Zeeman spectrum with Eq. (3) by setting $A_{m_F} = 0$, $\omega_s = 0$, $B = 460$ mG, and $t = 150$ ms in Fig. 2, and it agrees well with the experimental data.

When we tune the currents of TDCCs to decease the strength of the magnetic field, the splitting becomes less ob-

vious, and finally, all the peaks merge into a single broader peak. Although we can narrow the linewidth by further fine-tuning the TDCCs, the exact zero magnetic field still cannot be achieved. In order to further determine the strength of the residual magnetic field, we keep the clock-laser intensity unchanged and scan the clock-laser frequency under the 150-ms interrogation time, and the Rabi spectrum without driving is shown in Fig. 4. This narrow spectrum can be taken as the summation of contributions from all the sublevels with uniform atom distribution. Thus, we can determine the stray magnetic field B by fitting the experimental data with Eq. (3), taking $A_{m_F} = 0$, $\omega_s = 0$, and the Rabi frequencies of the sublevels determined before. As shown in Fig. 4, the fitting implies a residual magnetic field with $B = 6$ mG instead of zero.
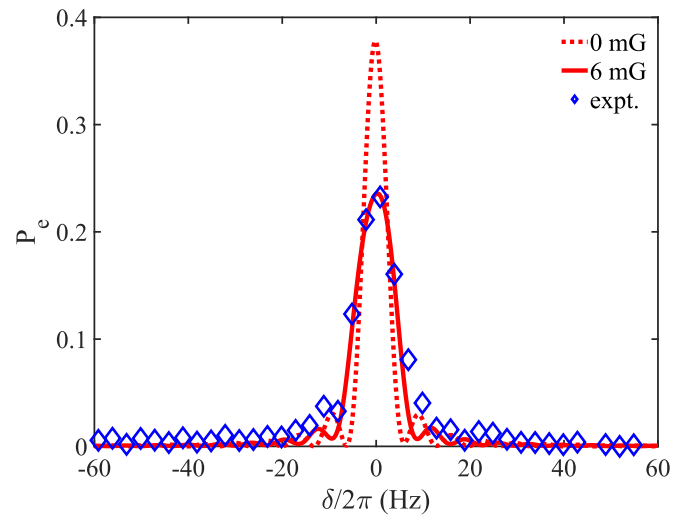

FIG. 4. The degenerate narrow spectrum at 150-ms clock-laser interrogation time. The blue diamonds are the experimental data. The solid and dashed lines are the theoretical results with magnetic field $B = 6$ mG and 0, respectively.
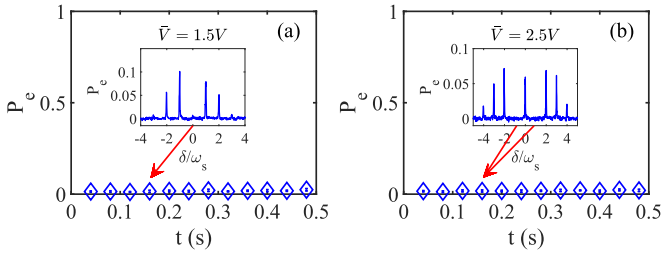
FIG. 5. Rabi oscillations of (a) the zeroth Floquet sideband at $\bar{V} = 1.5$ V and (b) the first Floquet sideband at $\bar{V} = 2.5$ V. The insets show the corresponding Rabi spectroscopy.

V. ANALYSIS OF THE SU(N) SYMMETRY

The experimental parameters obtained in the nondriven case are assumed to be unchanged even when introducing the periodic modulation, except for the atom distribution N_{m_F}/N_0 due to the possible SU(N) symmetry-breaking-induced atomic redistribution among these sublevels. Meanwhile, the renormalized driving amplitude A_{m_F} may also be different because the sublevels may have different velocities in the lattice comoving frame due to the periodic modulation [39].

First, it is easy to verify whether the renormalized driving amplitude is sublevel dependent. If driving amplitudes are different, the corresponding Bessel function $J_k(A_{m_F})$ cannot be fine-tuned simultaneously to zero for all sublevels, so that the excitation population of the kth-order Floquet sideband cannot be totally suppressed to zero. In the experiment, the renormalized driving amplitude A_{m_F} can be tuned by changing the voltages added to the PZT $\bar{V}$ [39]. As shown in the insets in Fig. 5, the zeroth (first) Floquet sideband of the Floquet Rabi spectroscopy is almost completely suppressed at $\bar{V} = 1.5$ V ($\bar{V} = 2.5$ V). To rule out the accidental case, we also measure the Rabi oscillation of these suppressed Floquet sidebands in Fig. 5. The experimental data clearly show that the excitation populations of both the zeroth Floquet sideband at $\bar{V} = 1.5$ V and the first one at $\bar{V} = 2.5$ V are almost zero up to 500 ms. They straightforwardly demonstrate all the renormalized driving amplitudes A_{m_F} are fine-tuned simultaneously to the same value and thus imply that A_{m_F} is sublevel independent. Thus, we can set the renormalized driving amplitudes of all sublevels to be the same value, $A_{m_F} = A(\bar{V})$ at voltage $\bar{V}$.

Then, we turn to the atom distribution N_{m_F}/N_0. In order to extract N_{m_F}/N_0, we experimentally measure the Rabi spectrum at different voltages and fit them according to Eq. (3) by taking N_{m_F}/N_0 and $A(\bar{V})$ as free parameters. Here the contributions of P_e at sublevel $m_F = \pm 1/2$ are ignored because the corresponding Rabi frequency is too small. In addition, N_{m_F}/N_0 is assumed to be irrelevant to the sign of m_F. With this fitting method, we got the Rabi spectrum (see Fig. 6), the relation between the voltage and A (see Fig. 7), and the atomic distribution among the sublevels (see Fig. 8). We will give a concrete analysis of them in the following.

In Fig. 6, we show the experimental data for the degenerate Floquet Rabi spectroscopy compared with the theoretical results at different driving voltages. Generally, the theoretical results are in good agreement with the experiments at all
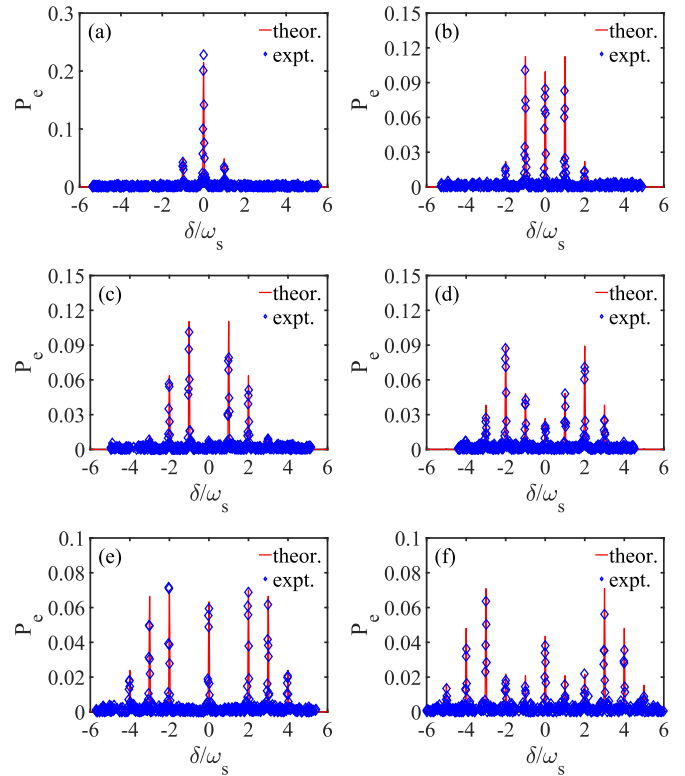

FIG. 6. The Floquet degenerate spectrum at 150-ms clock-laser interrogation time, driving frequency $\omega_s/2\pi = 200$ Hz, and residual magnetic field $B = 6$ mG. The experimental data (blue diamonds) are compared to the theoretical results (red solid lines) at the driving voltages (a) $\bar{V} = 0.5$ V, (b) $\bar{V} = 1.0$ V, (c) $\bar{V} = 1.5$ V, (d) $\bar{V} = 2.0$ V, (e) $\bar{V} = 2.5$ V, and (f) $\bar{V} = 3.0$ V.

driving voltages. The intervals between the Floquet sidebands are the same as the driving frequency ω_s. Actually, some small deviations exist because the Floquet spectra are obtained by
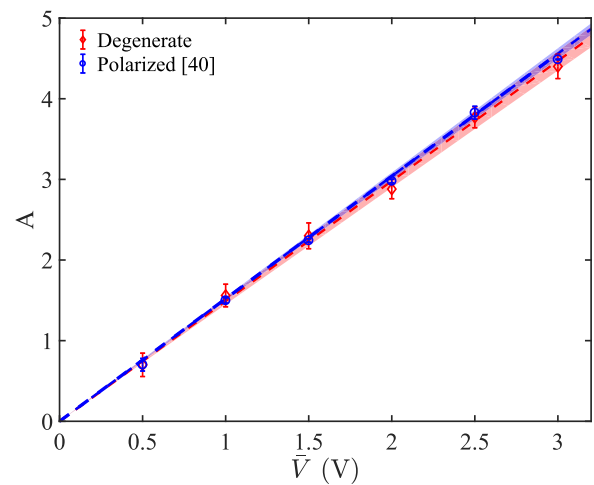

FIG. 7. The relationship between the renormalized driving amplitude A and driving voltage $\bar{V}$ added to the PZT in the Floquet degenerate system (red diamonds) and the Floquet polarized system (blue circles, from Ref. [39]). The dashed lines are linear fitting results, and the red region shows the 1σ deviation from the fitting line of the Floquet degenerate results.
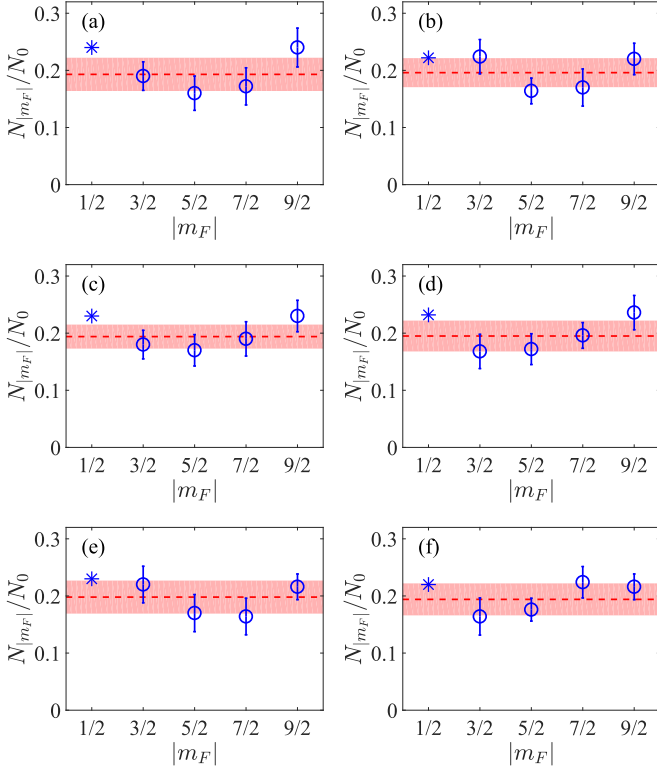
FIG. 8. The atomic distribution at different sublevels obtained by fitting the experimental data with Eq. (3) from Floquet theory. The voltages added to the PZT are (a) $\bar{V} = 0.5$ V, (b) $\bar{V} = 1.0$ V, (c) $\bar{V} = 1.5$ V, (d) $\bar{V} = 2.0$ V, (e) $\bar{V} = 2.5$ V, and (f) $\bar{V} = 3.0V$. The dashed lines indicate the weighted mean, and the red region shapes the 1σ standard deviation. The atomic distribution at sublevel $m_F = 1/2$ labeled with a star is calculated by subtracting the other sublevels from 1.

scanning the clock laser with a step of 3 Hz, so it may fail to touch the peaks of all Floquet sidebands with linewidths of a few hertz.

In a previous work [39], the relation between the driving amplitude A and the voltage $\bar{V}$ added to the PZT is linear. Before investigating the atom distribution, it is better to verify the linear relation between A and $\bar{V}$. Figure 7 demonstrates the slope of the degenerate case is very close to the polarized one (all atoms are pumped into the sublevels $m_F = \pm 9/2$) and thus verifies the linearity. Indeed, after linearly fitting the data with $A = k\bar{V}$, we obtain the coefficient $k = 1.49(4)/V$, which is approximately the same as the polarized case with $k = 1.52/V$ [39].

Finally, as the most critical aspect, the atomic distributions extracted by fitting the experiment data are shown in Fig. 8. Clearly, they are different, and a few more atoms stay at some sublevels, such as $m_F = \pm 9/2$. However, most of them fall into the 1σ standard deviation of the weighted mean value (red region around 1/5). The distribution in $m_F = \pm 1/2$ is obtained by subtracting the atoms in other sublevels from unity. It is always larger than 1/5, which may result from neglecting the population on $m_F = \pm 1/2$ due to the small Rabi frequency. Based on these experimental results, we conclude that periodic driving will not break the SU(N) symmetry in a certain accuracy range.

VI. CONCLUSIONS AND DISCUSSION

In this work, we experimentally studied the Rabi spectroscopy of a degenerate OLC system under FE. Although the residual stray magnetic field cannot be eliminated, we can still check whether the SU(N) symmetry is broken by the FE. We found that the driving amplitude and its relationship with the voltage added to the PZT are independent of the Zeeman sublevels, which implies that the trapping potential is independent of the nuclear spin even with FE. More importantly, the atomic population among the sublevels is still almost uniform, which implies that the interatomic collision is independent of nuclear spin under FE.

Although SU(N) symmetry breaking cannot be completely ruled out, our experiments still support the idea that periodic modulation of the lattice frequency will not have an obvious influence on the SU(N) symmetry. Our work provides a paradigm using ultranarrow spectroscopy to verify the SU(N) symmetry, which may be extended to verify the SU(N) symmetry in many-body systems. In addition, our work may provide a flexible way to quantum control the multilevel nuclear spin [58,59], which is useful for universal qudit-based quantum computing. FE combined with SU(N) physics can also be used to study SU(N) topological insulators with high winding numbers, which can be expected to enlarge the scope of symmetry-protected topology [40]. When extended to many-body scenarios, FE can be used to renormalize the SU(N) Hubbard model to touch the various phases of matter. For instance, one can simultaneously tune the Bloch bands for all the sublevels to study exotic SU(N) phases in the shallow lattice [10,38,57]. In conclusion, our work will not only benefit the Floquet OLC [57] but also shed light on using the degenerate AEA OLC for quantum computing and quantum simulation [60,61].

APPENDIX

Here we determine the experimental parameters (listed in Table I) using the motional sideband spectrum without driving (one can also refer to Ref. [46] for an elaborate theoretical
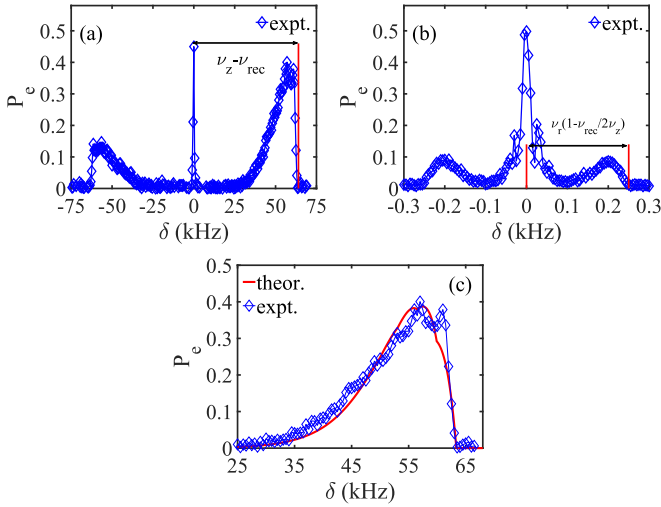
FIG. 9. Determination of the experimental parameters in the non-driven case. (a) The experimental data for the motional sideband spectrum in the z direction. (b) The experimental data for the motional sideband spectrum in the r direction. (c) Theoretical fitting (red line) with experimental data (blue diamonds) for the blue sideband in the z direction.

description). The motional trap frequencies [the longitudinal (transverse) trap frequency ν_z (ν_r)], the numbers of motional states (N_z and N_r), and the atom temperatures (T_z and T_r) are what we prepare to determine in this Appendix. The motional sideband spectrum is obtained by changing the frequency of the clock laser with a step of 500 Hz around the clock-transition frequency, as shown in Fig. 9(a). The intensity of the clock laser is about $0.5\,\mathrm{W/cm^2}$, and the carrier peak is about 1 kHz due to the saturation broadening. The complicated sideband spectrum indicates that we need a subtler description of the energy spectrum more than a simple harmonic trap. By approximating the longitudinal potential as a 1D harmonic trap with a quartic distortion and the transverse potential as a two-dimensional harmonic trap, we get the longitudinal blue-sideband energy gap, which means the motional transition $|n_r, n_z\rangle \to |n_r, n_z + 1\rangle$ [46],

$$\gamma(n_z) = \nu_z - \nu_{\rm rec}(n_z + 1) - \nu_{\rm rec}\frac{\nu_r}{\nu_z}(n_r + 1). \qquad (A1)$$

Similarly, we get the transverse motional sideband spectrum when there is a slight angle between the clock and lattice laser beam. And the power of the clock laser is reduced to about 10 μW to get the transverse resolved sideband spectrum shown in Fig. 9(b). So the transverse blue-sideband energy gap, which means the motional transition $|n_r, n_z\rangle \to |n_r + 1, n_z\rangle$, is

$$\gamma(n_r) = \nu_r - \nu_{\rm rec}\frac{\nu_r}{\nu_z}(n_z + 1/2). \qquad (A2)$$

The position of the longitudinal blue-sideband sharp edge means that the largest energy gap determines the longitudinal trapping frequency ν_z by $\gamma(n_z)(n_z = 0, n_r = 0) \simeq \nu_z - \nu_{\rm rec}$. Similarly, we can determine the transverse trapping frequency by $\gamma(n_r)(n_z = 0) = \nu_r - \nu_{\rm rec}\nu_r/2\nu_z$. Thus, we can see from Figs. 9(a) and 9(b) that $\nu_z = 66.8$ kHz and $\nu_r = 250$ Hz. Then we can determine the trap depth and the beam waist by $U_0 = \nu_z^2 E_R/4\nu_{\rm rec}^2 \simeq 94\ E_R$ and $w_0 = \sqrt{U_0/m\nu_r^2\pi^2} = 49$ μm, and the number of motional states is $N_z \simeq U_0/h\nu_z = 5$ and $N_r \simeq U_0/h\nu_r = 1336$. Now we determine the atom temperature. The longitudinal red sideband means the motional transition $|n_r, n_z\rangle \to |n_r, n_z - 1\rangle$. If we disregard the details of the sideband line shapes, the only difference between the blue and red sidebands is that the Boltzmann weights are shifted according to $n_z \to n_z + 1$. And the longitudinal ground state $n_z = 0$ dose not contribute to the red sideband, so we can determine the longitudinal temperature with the ratio of sideband cross sections,

$$\frac{\sigma_{\rm red}}{\sigma_{\rm blue}} = \frac{\sum_{n_z=1}^{N_z} q(n_z)}{\sum_{n_z=0}^{N_z-1} q(n_z)}, \qquad (A3)$$

which gives us the longitudinal temperature $T_z = 3.5$ μK. The transverse temperature can be extracted from the longitudinal blue-sideband line shape with [46]

$$\sigma_{\rm blue}(\delta) \propto \sum_{n_z=0}^{N_z-1} q(n_z)\frac{\alpha\tilde{\delta}}{\tilde{\gamma}(n_z)}e^{-\alpha\tilde{\delta}}\Theta[\tilde{\gamma}(n_z)\tilde{\delta}], \qquad (A4)$$

where $\alpha = [\tilde{\gamma}(n_z)/\nu_{\rm rec}](h\nu_z/k_B T_r)$, $\tilde{\gamma}(n_z) = \nu_z - \nu_{\rm rec}(n_z + 1)$, $\tilde{\delta} = 1 - \delta/\tilde{\gamma}(n_z)$, and Θ is the Heaviside function. By fitting with experimental data [Fig. 9(c)], we get the transverse temperature $T_r = 4.0$ μK.

---

[1] A. D. Ludlow, M. M. Boyd, J. Ye, E. Peik, and P. O. Schmidt, Rev. Mod. Phys. **87**, 637 (2015).

[2] B. J. Bloom, T. L. Nicholson, J. R. Williams, S. L. Campbell, M. Bishof, X. Zhang, W. Zhang, S. L. Bromley, and J. Ye, Nature (London) **506**, 71 (2014).

[3] T. L. Nicholson, S. L. Campbell, R. B. Hutson, G. E. Marti, B. J. Bloom, R. L. McNally, W. Zhang, M. D. Barrett, M. S. Safronova, G. F. Strouse, W. L. Tew, and J. Ye, Nat. Commun. **6**, 6896 (2015).

[4] T. Bothwell, D. Kedar, E. Oelker, J. Robinson, S. Bromley, W. Tew, J. Ye, and C. Kennedy, Metrologia **56**, 065004 (2019).

[5] G. E. Marti, R. B. Hutson, A. Goban, S. L. Campbell, N. Poli, and J. Ye, Phys. Rev. Lett. **120**, 103201 (2018).

[6] C. Wu, Mod. Phys. Lett. B **20**, 1707 (2006).

[7] A. V. Gorshkov, M. Hermele, V. Gurarie, C. Xu, P. S. Julienne, J. Ye, P. Zoller, E. Demler, M. D. Lukin, and A. M. Rey, Nat. Phys. **6**, 289 (2010).

[8] G. Pagano, M. Mancini, G. Cappellini, P. Lombardi, F. Schäfer, H. Hu, X.-J. Liu, J. Catani, C. Sias, M. Inguscio, and L. Fallani, Nat. Phys. **10**, 198 (2014).

[9] F. Scazza, C. Hofrichter, M. Höfer, P. C. De Groot, I. Bloch, and S. Fölling, Nat. Phys. **10**, 779 (2014).

[10] M. A. Cazalilla and A. M. Rey, Rep. Prog. Phys. **77**, 124401 (2014).

[11] X. Zhang, M. Bishof, S. L. Bromley, C. V. Kraus, M. S. Safronova, P. Zoller, A. M. Rey, and J. Ye, Science **345**, 1467 (2014).

[12] M. E. Beverland, G. Alagic, M. J. Martin, A. P. Koller, A. M. Rey, and A. V. Gorshkov, Phys. Rev. A **93**, 051601(R) (2016).

[13] G. Chen, K. R. A. Hazzard, A. M. Rey, and M. Hermele, Phys. Rev. A **93**, 061601(R) (2016).

[14] D. Banerjee, M. Bögli, M. Dalmonte, E. Rico, P. Stebler, U.-J. Wiese, and P. Zoller, Phys. Rev. Lett. **110**, 125303 (2013).

[15] M. A. Perlin and A. M. Rey, New J. Phys. **21**, 043039 (2019).

[16] C. He, E. Hajiyev, Z. Ren, B. Song, and G.-B. Jo, J. Phys. B **52**, 102001 (2019).

[17] S. Choudhury, K. R. Islam, Y. Hou, J. A. Aman, T. C. Killian, and K. R. A. Hazzard, Phys. Rev. A **101**, 053612 (2020).

[18] C. Wu, J.-P. Hu, and S.-C. Zhang, Phys. Rev. Lett. **91**, 186402 (2003).

[19] C. Wu, Nat. Phys. **8**, 784 (2012).

[20] C. Wu, Physics **3**, 92 (2010).

[21] G. Chen and C. Wu, arXiv:2112.02630.

[22] C. Honerkamp and W. Hofstetter, Phys. Rev. Lett. **92**, 170403 (2004).

[23] M. Hermele, V. Gurarie, and A. M. Rey, Phys. Rev. Lett. **103**, 135301 (2009).

[24] M. Hermele and V. Gurarie, Phys. Rev. B **84**, 174441 (2011).

[25] M. A. Cazalilla, A. F. Ho, and M. Ueda, New J. Phys. **11**, 103033 (2009).

[26] S. Stellmer, R. Grimm, and F. Schreck, Phys. Rev. A **84**, 043611 (2011).

[27] S. Taie, R. Yamazaki, S. Sugawa, and Y. Takahashi, Nat. Phys. **8**, 825 (2012).

[28] G. Cappellini, M. Mancini, G. Pagano, P. Lombardi, L. Livi, M. Siciliani de Cumis, P. Cancio, M. Pizzocaro, D. Calonico, F. Levi, C. Sias, J. Catani, M. Inguscio, and L. Fallani, Phys. Rev. Lett. **113**, 120402 (2014).

[29] A. Eckardt, Rev. Mod. Phys. **89**, 011004 (2017).

[30] A. Zenesini, H. Lignier, D. Ciampini, O. Morsch, and E. Arimondo, Phys. Rev. Lett. **102**, 100403 (2009).

[31] N. R. Cooper, J. Dalibard, and I. B. Spielman, Rev. Mod. Phys. **91**, 015005 (2019).

[32] G. Jotzu, M. Messer, R. Desbuquois, M. Lebrat, T. Uehlinger, D. Greif, and T. Esslinger, Nature (London) **515**, 237 (2014).

[33] M. Aidelsburger, M. Lohse, C. Schweizer, M. Atala, J. T. Barreiro, S. Nascimbène, N. R. Cooper, I. Bloch, and N. Goldman, Nat. Phys. **11**, 162 (2015).

[34] M. Aidelsburger, M. Atala, M. Lohse, J. T. Barreiro, B. Paredes, and I. Bloch, Phys. Rev. Lett. **111**, 185301 (2013).

[35] J. Struck, C. Ölschläger, M. Weinberg, P. Hauke, J. Simonet, A. Eckardt, M. Lewenstein, K. Sengstock, and P. Windpassinger, Phys. Rev. Lett. **108**, 225304 (2012).

[36] J. Struck, M. Weinberg, C. Ölschläger, P. Windpassinger, J. Simonet, K. Sengstock, R. Höppner, P. Hauke, A. Eckardt, M. Lewenstein, and L. Mathey, Nat. Phys. **9**, 738 (2013).

[37] H. Miyake, G. A. Siviloglou, C. J. Kennedy, W. C. Burton, and W. Ketterle, Phys. Rev. Lett. **111**, 185302 (2013).

[38] R. Zhang, Y. Cheng, P. Zhang, and H. Zhai, Nat. Rev. Phys. **2**, 213 (2020).

[39] M.-J. Yin, T. Wang, X.-T. Lu, T. Li, Y.-B. Wang, X.-F. Zhang, W.-D. Li, A. Smerzi, and H. Chang, Chin. Phys. Lett. **38**, 073201 (2021).

[40] X.-T. Lu, T. Wang, T. Li, C.-H. Zhou, M.-J. Yin, Y.-B. Wang, X.-F. Zhang, and H. Chang, Phys. Rev. Lett. **127**, 033601 (2021).

[41] W.-X. Liu, T. Wang, X.-F. Zhang, and W.-D. Li, Phys. Rev. A **104**, 053318 (2021).

[42] M. P. Silveri, J. A. Tuorila, E. V. Thuneberg, and G. S. Paraoanu, Rep. Prog. Phys. **80**, 056002 (2017).

[43] R. H. Dicke, Phys. Rev. **89**, 472 (1953).

[44] T. Mukaiyama, H. Katori, T. Ido, Y. Li, and M. Kuwata-Gonokami, Phys. Rev. Lett. **90**, 113002 (2003).

[45] M. Takamoto and H. Katori, Phys. Rev. Lett. **91**, 223001 (2003).

[46] S. Blatt, J. W. Thomsen, G. K. Campbell, A. D. Ludlow, M. D. Swallows, M. J. Martin, M. M. Boyd, and J. Ye, Phys. Rev. A **80**, 052703 (2009).

[47] Y.-B. Wang, M.-J. Yin, J. Ren, Q.-F. Xu, B.-Q. Lu, J.-X. Han, Y. Guo, and H. Chang, Chin. Phys. B **27**, 023701 (2018).

[48] W. Nagourney, J. Sandberg, and H. Dehmelt, Phys. Rev. Lett. **56**, 2797 (1986).

[49] M. M. Boyd, T. Zelevinsky, A. D. Ludlow, S. Blatt, T. Zanon-Willette, S. M. Foreman, and J. Ye, Phys. Rev. A **76**, 022510 (2007).

[50] C. Shi, J.-L. Robyr, U. Eismann, M. Zawada, L. Lorini, R. Le Targat, and J. Lodewyck, Phys. Rev. A **92**, 012516 (2015).

[51] P. G. Westergaard, J. Lodewyck, L. Lorini, A. Lecallier, E. A. Burt, M. Zawada, J. Millo, and P. Lemonde, Phys. Rev. Lett. **106**, 210801 (2011).

[52] A. Lurio, M. Mandel, and R. Novick, Phys. Rev. **126**, 1758 (1962).

[53] A. Brusch, R. Le Targat, X. Baillard, M. Fouché, and P. Lemonde, Phys. Rev. Lett. **96**, 103003 (2006).

[54] X. Baillard, M. Fouché, R. L. Targat, P. G. Westergaard, A. Lecallier, Y. L. Coq, G. D. Rovera, S. Bize, and P. Lemonde, Opt. Lett. **32**, 1812 (2007).

[55] I. Ushijima, M. Takamoto, and H. Katori, Phys. Rev. Lett. **121**, 263202 (2018).

[56] M. M. Boyd, A. D. Ludlow, S. Blatt, S. M. Foreman, T. Ido, T. Zelevinsky, and J. Ye, Phys. Rev. Lett. **98**, 083002 (2007).

[57] M.-J. Yin, X.-T. Lu, T. Li, J.-J. Xia, T. Wang, X.-F. Zhang, and H. Chang, Phys. Rev. Lett. **128**, 073603 (2022).

[58] S. Omanakuttan, A. Mitra, M. J. Martin, and I. H. Deutsch, Phys. Rev. A **104**, L060401 (2021).

[59] P. J. Low, B. M. White, A. A. Cox, M. L. Day, and C. Senko, Phys. Rev. Res. **2**, 033128 (2020).

[60] A. J. Daley, M. M. Boyd, J. Ye, and P. Zoller, Phys. Rev. Lett. **101**, 170504 (2008).

[61] A. J. Daley, Quantum Inf. Process. **10**, 865 (2011).